Comparison of the Low and High/Very High Cycle Fatigue Behaviors in Ni Microbeams under Bending

Alejandro Barrios[1], Ebiakpo Kakandar[2], Gustavo Castelluccio[2] and Olivier Pierron[1]

[1]G.W. Woodruff School of Mechanical Engineering, Georgia Institute of Technology, Atlanta, GA, 30332-0405, USA

[2]School of Aerospace, Transport, and Manufacturing, Cranfield University, Bedfordshire MK43 0AL, UK

Abstract

The present work demonstrates a micromechanical technique to investigate the Low Cycle Fatigue (LCF) behavior of Ni microbeams under fully reversed bending loadings. The technique extends the range of measured fatigue lives from the previously reported technique for High and Very High Cycle Fatigue (HCF/VHCF) characterization in the same microbeams. The results highlight significant differences in the slope of stress and strain-life behavior and crack propagation rates that differ from an average of 10^{-12} m/cycle in HCF/VHCF to an average of 10^{-8} m/cycle in LCF. These results, in addition to *postmortem* fractography work, suggest that the mechanisms follow the conventional mechanisms of crack tip stress intensification in the LCF regime. This is in stark contrast to the void controlled mechanisms that were previously identified in the HCF/VHCF regime. These results demonstrate that the transition in governing mechanisms from void controlled to conventional mechanisms is highly influenced by the size effects present in the microbeams.

1   Introduction

Over the past 30 years, the study of the fatigue behavior of small-scale materials has become of great importance due to the technological drive to transition from bulk traditional engineering structures to micro/nano structures [1-3]. Many of these micrometer-scale structures and metallic films have been prominently used in recent years and encompass a wide range of applications. For example, microelectromechanical systems (MEMS) have been used as a variety of sensors, ranging from accelerometers and gyroscopes to biotechnology and chemical sensors [3-7]. More specifically, fatigue failure is of paramount importance to these structures due to the high number of movable components that are exposed to repeated loadings for a great number of cycles. Fatigue mechanisms in bulk materials are mostly well understood [8, 9] but small-scale materials exhibit a particular behavior due to the presence of size effects. Therefore, more advanced and specific techniques are required to study their fatigue behavior. Many micro and nanomechanical techniques have been adopted to investigate metallic micrometer-scale structures under fatigue loadings appropriate to their applications [10-23].

Pierron and co-workers have extensively studied the fatigue behavior of Ni microbeams under fully reversed bending loadings in the High Cycle and Very High Cycle Fatigue (HCF/VHCF) [24-28]. More recently, they have introduced a quantitative *in-situ* scanning electron microscope (SEM) nanoscale investigation of the Ni microbeams in the HCF/VHCF regimes under bending [29] using a microresonator technique (see Section 4.2). Results from the *in-situ* technique highlighted strong environmental and size effects with unusual fatigue behavior in the stress-life curve and ultra-slow crack propagation rates of the order of 10^{-12} m/cycle, suggesting that fatigue crack growth is not a continuous process. Focused Ion Beam (FIB) cross-sections revealed that the nanoscale fatigue mechanism in the HCF/VHCF regime does not follow the conventional

mechanism of crack tip stress intensification. Instead, the nucleation and propagation mechanisms are controlled by the nucleation of voids (resulting from vacancy condensation processes) underneath extrusions or ahead of the crack tip. Additionally, the strong environmental effects and the observation of voids in subsurface areas and near the crack tip suggest that the diffusion of oxygen or water is essential for the formation of voids. This void dominated fatigue process is thought to be a consequence of the reduction in driving force for crack growth caused by the effects of extreme stress gradients [29]. Therefore, we hypothesized that the conditions applied in HCF/VHCF are below a threshold limit for the conventional mechanisms to operate. Consequently, the application of larger strains amplitudes (larger driving force) to these microbeams is expected to result in a transition in the governing fatigue mechanisms.

In this paper, the fatigue behavior of the same Ni microbeams are further investigated under the Low Cycle Fatigue (LCF) regime. A micromechanical external actuation technique was developed in order to test microbeams at higher applied strain amplitudes and lower fatigue lives than what was possible using the resonance method. The propagation rates, fatigue properties and nanoscale mechanisms can be analyzed over a wide range of applied strain amplitudes and comparisons can be traced between the LCF and the HCF/VHCF regimes. In addition, the study of frequency effects on the fatigue lives of the microbeams can be investigated by contrasting results at similar strain amplitudes from the two techniques which employ significantly different frequencies.

2   Results and Discussion

2.1   LCF Test Examples

The change in load amplitude throughout a fatigue test was evaluated for a number of microbeams deformed at different plastic strains using the external actuation technique. Figure 1(a) shows the evolution in load amplitude applied to the microbeam as a function of cycles for a test performed

at 79 mrad rotation and an estimated σ_a = 715 MPa and ε_a = 0.96% (see Section 4.4). The load

amplitude decreases steadily until ~600 cycles (15% decrease in load amplitude) and then shows

a rapid decrease due to the propagation of cracks, reaching the failure threshold at N_f = 680 cycles.

The *postmortem* images of the microbeam are shown in Figure 1(b) and (c), where through

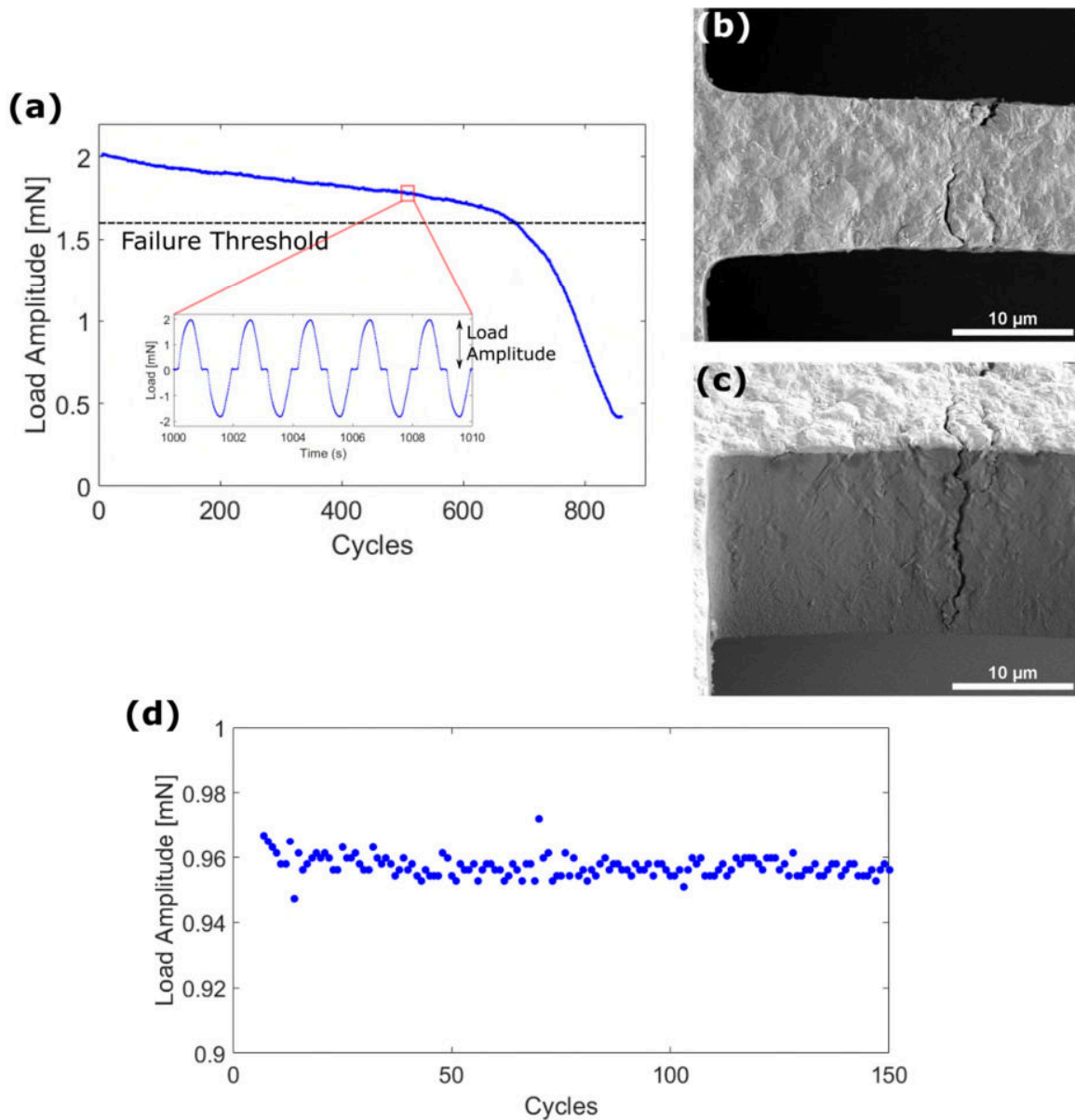thickness cracks and extrusions/intrusions are observed on both sides of the microbeam.

Figure 1. (a) Load amplitude evolution of a test performed at 79 mrad rotation (estimated σ_a = 715 MPa and ε_a = 0.96%); (b) and (c) Top and side views of failed microbeam; (d) First 150 cycles of microbeam tested at 22 mrad rotation (estimated σ_a = 430 MPa and ε_a = 0.26%)

Figure 1(d) shows results from the first 150 cycles from another microbeam tested at 22 mrad rotation with an estimated σ_a = 430 MPa, ε_a = 0.26% and N_f = 3.4×10^5 cycles. Both the load amplitude and the angle of rotation stay approximately constant, suggesting that there is no perceivable cyclic hardening or softening behavior.

Microstructural sensitive models were also developed to further investigate the role of the microstructure on the stress/load response. Following the same crystal plasticity approach presented before [25, 30], we computed the stress response of the microbeam which is heterogeneous due to the microstructure (Figure 2(a) and (b)). Furthermore, Figure 2(c) presents the nodal force required to bend the beam as a function of the rotation angle computed from simulations with isotropic elasto-plastic models [25, 30].
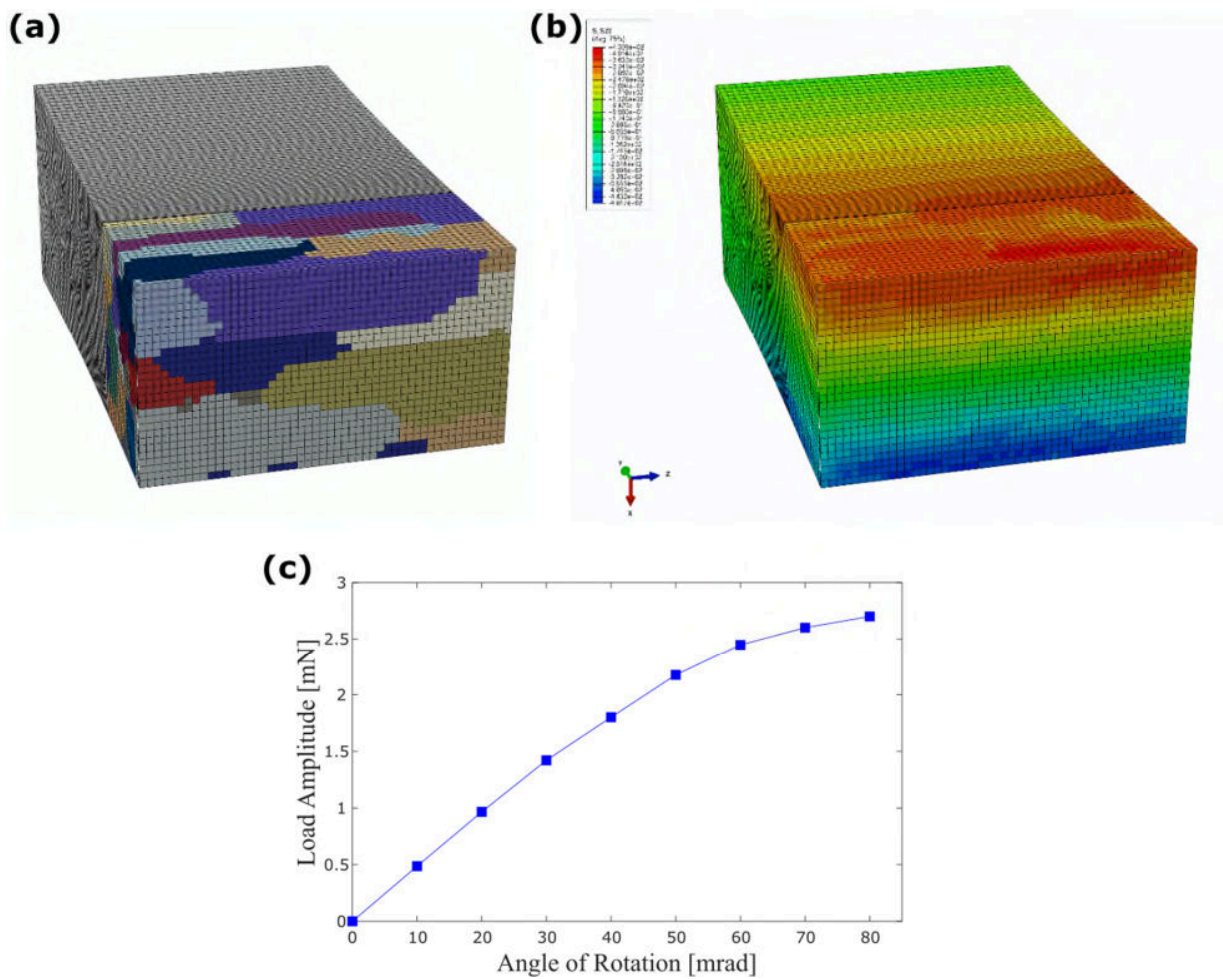
Figure 2. Partial cut of the microbeam model showing (a) the microstructure and (b) the stress along the axial direction computed from crystal plasticity simulations [25, 30] in a microbeam rotated by 30 mrad. Note the heterogeneous distribution due to the microstructure and the neutral axis; (c) Rotation force reaction as a function of the angle of rotation computed from simulations with isotropic elasto-plastic models [25, 30]

The load values in Figure 1 are in agreement with the modelling results in Figure 2 when considering the uncertainties in the exact loading point in experiments and the boundary conditions

in models. Overall, these results confirm the assumptions in prior efforts [25, 28] that the monotonic and cyclic behavior of these Ni microbeams are similar in the HCF/VHCF regime.

In the microbeam tested at 22 mrad rotation ($\varepsilon_a = 0.26\%$), the nucleation of a fatigue crack is expected to occur after ~ 2.5×10^5 cycles in air, based on previous observations of crack nucleation in the HCF/VHCF regime (2-4% decrease in f_o or 4-8% decrease in load amplitude) [29]. However, in the sample tested at 79 mrad rotation ($\varepsilon_a = 0.96\%$), an 8% decrease in load amplitude happens at only ~300 cycles, revealing that cracks nucleate much faster in the LCF regime.

2.2 Stress-Life Curves

The stress and strain life curves were evaluated for both studied regimes and are shown in Figure 3(a) and (b), respectively. The external actuation technique allowed for fatigue tests to be performed ranging from 400 to 715 MPa in σ_a and from 0.25% to 0.96% in ε_a, while previously reported tests with the electrostatic technique range from 200 to 450 MPa in σ_a and from 0.01% to 0.28% in ε_a. Therefore, with the two techniques the microbeams were tested over six orders of magnitude in fatigue lives. In Figure 3, empty symbols denote the runout specimens and solid symbols represent fatigue failure.
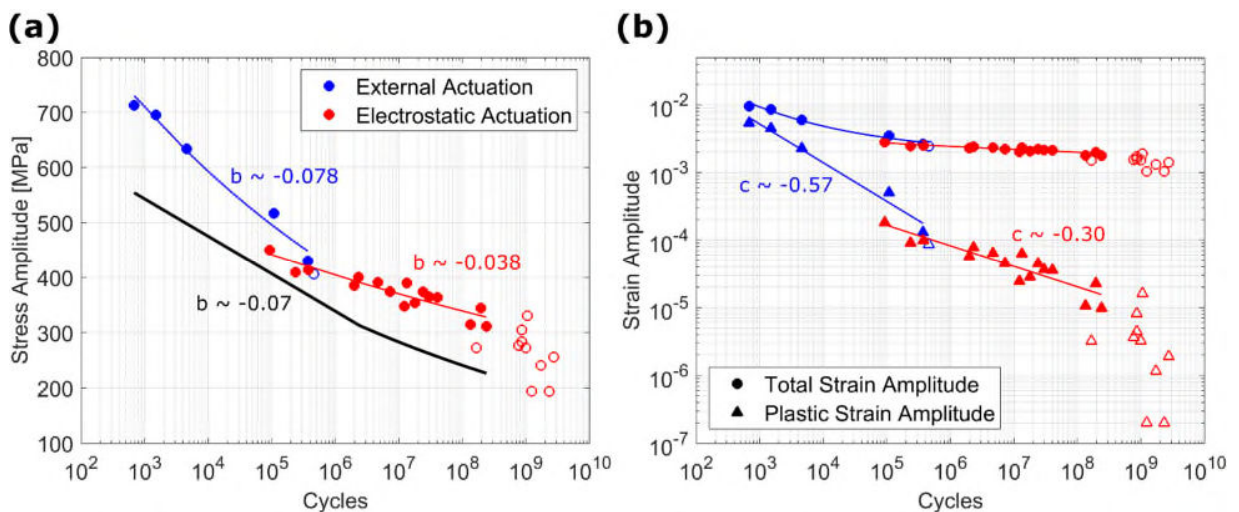
Figure 3. (a) Stress and (b) Strain life curves for the LCF and HCF/VHCF. Solid black line in (a) represents the fatigue behavior of electroplated Ni films in the absence of strain gradients [31]

Both the LCF and HCF/VHCF regimes were fitted with life prognosis laws from Basquin (Equation 1) and Coffin-Manson (Equation 2) [9] below:

$$\sigma_a = \sigma_f'(2N_f)^b \qquad\qquad (1)$$

$$\varepsilon_{pa} = \varepsilon_f'(2N_f)^c \qquad\qquad (2)$$

where σ_f' is the fatigue strength coefficient, b is the Basquin exponent, ε_f' is the fatigue ductility coefficient and c is the Coffin Manson coefficient; and show good correlations with the power fits. The Basquin exponent changes from -0.038 in the HCF/VHCF to -0.078 in the LCF regime, while the Coffin-Manson coefficient changes from -0.30 in the HCF/VHCF to -0.57 in the LCF regime The LCF regime presents a Basquin coefficient closer to behavior of electroplated Ni films under the absence of stress/strain gradients, which has b~ -0.07 (also shown in Figure 3(a)) [31] and a Coffin Manson coefficient closer to typical values for bulk metals, which show c values ranging from -0.5 to -0.8 [9]. Overall, the fatigue curves change from a shallower behavior in the HCF/VHCF to a more conventional behavior in the LCF regime. The significant change in fatigue properties and behavior suggest that there is a change in the physical mechanisms for crack nucleation and propagation caused by the increase in applied strain amplitude. Therefore, the dominating fatigue mechanism may no longer be the void controlled mechanisms reported for the HCF/VHCF regime [29].

The overlapping fatigue curves shown in Figure 3 which were obtained at two different frequencies (0.5 Hz vs 8 kHz) suggest that there is no significant internal heating in our specimens during VHCF testing, unlike what can be observed in bulk metals [32, 33]. This is an expected result

given the microscopic size of the microbeams, as we have previously demonstrated using the known temperature dependence of resonance frequency [25, 27, 29]. The following section looks further at the lack of frequency effects.

2.3 Frequency Effects

The frequency effects on fatigue lives were investigated by employing the two techniques at similar stress and strain amplitudes. Figure 4(a) shows the plot of the normalized load amplitude $\left(\frac{N_a}{N_{initial}}\right)$ or resonance frequency $\left(\frac{f}{f_{initial}}\right)$ as a function of cycles, comparing two experiments with the different techniques. One sample was tested at 21 mrad ($\sigma_a = 415$ MPa and $\varepsilon_a = 0.25\%$) with $N_f = 3.8 \times 10^5$ using the electrostatic technique (frequency of ~ 8 kHz) and had a total runtime about 1 minute. The other sample was tested at 22 mrad ($\sigma_a = 430$ MPa and $\varepsilon_a = 0.26\%$) with $N_f = 3.4 \times 10^5$ using the external actuation technique (frequency of 0.5 Hz) and had a total runtime 9 days. Sidewall images of both microbeams after the fatigue tests are shown in Figure 4(b) and (c). Both microbeams sidewalls exhibit cracks and similar extrusion/intrusion densities. Both tests, ran at frequencies that differ by four orders of magnitude but at similar stress/strain amplitude, failed at approximately the same number of cycles, indicating that frequency does not play a significant role in the fatigue life of these Ni microbeams.
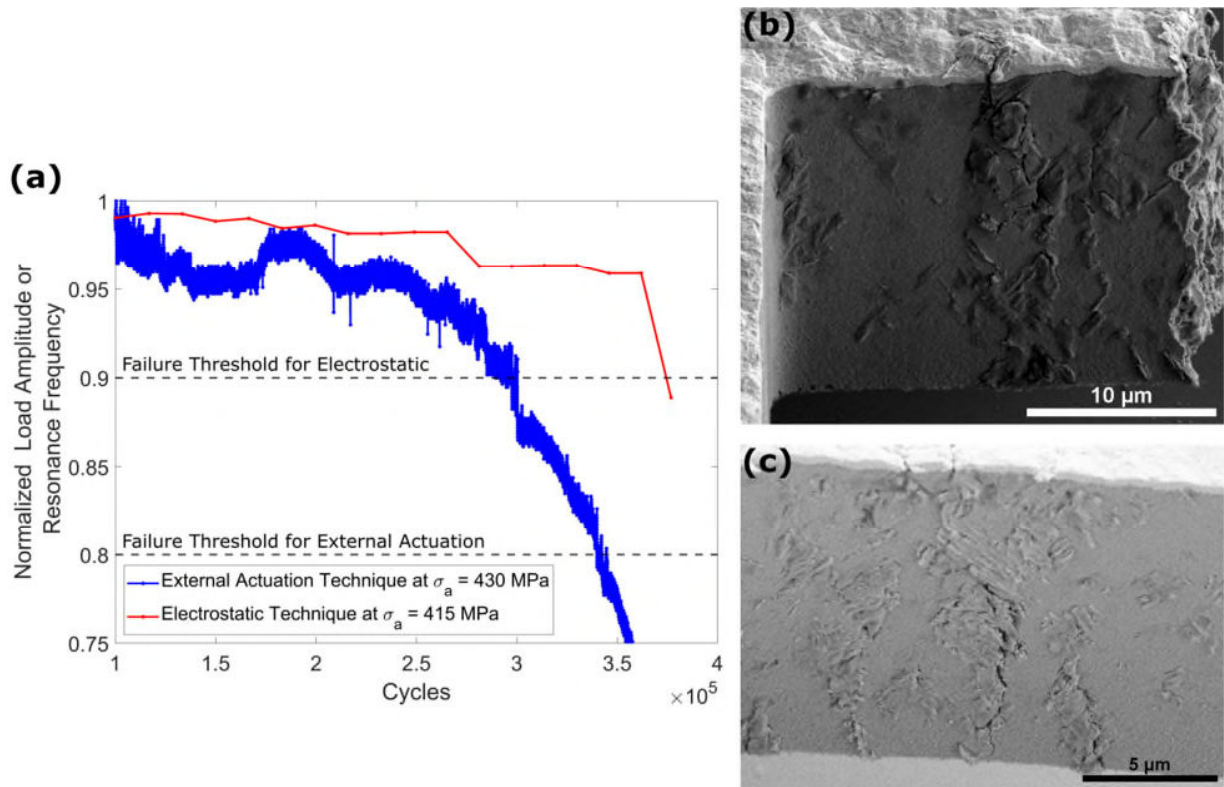
Figure 4. (a) Frequency and load amplitude evolution curves for sample tested with the two techniques; (b) Sidewall image of the sample tested at 22 mrad (estimated σ_a = 430 MPa and ε_a = 0.26%) with the external actuation technique; (c) Sidewall image of the sample tested at 21 mrad (estimated σ_a = 415 MPa and ε_a = 0.25%) with the electrostatic technique

2.4 Crack Propagation Rates

The effect of the applied strain amplitude was further investigated in regards to the crack propagation rates. The local crack propagation rates were measured for 2D cracks (one crack for each side of the microbeam) which spanned the entire thickness of the microbeam. Therefore, by observing crack evolution at the top surface of the microbeam through SEM images and by counting the number cycles in between two stages of a fatigue test, the average crack growth rates can be found [29]. Figure 5 shows *postmortem* images of the microbeam tested at 79 mrad (σ_a =

715 MPa, ε_a = 0.96%) and with N_f = 680 cycles (same microbeam shown in Figure 1(a)-(c)). The average crack growth rate in between the beginning and the end of the fatigue test was found to be $\frac{da}{dN} = 12\ nm/cycle$ ($da = 10\ \mu m$ and $dN = 850$ cycles). In addition, Figure 5(b) shows a transverse FIB cross-section exactly through the crack highlighted in Figure 5(a). The high-resolution SEM image at the cross-section, shown in Figure 5(c), reveal striations along the path of the crack towards the neutral axis of the microbeam. These fatigue striations are at an average distance d = 19 nm apart which is equivalent to an average crack growth rate of $\frac{da}{dN} = 19$ nm/cycle
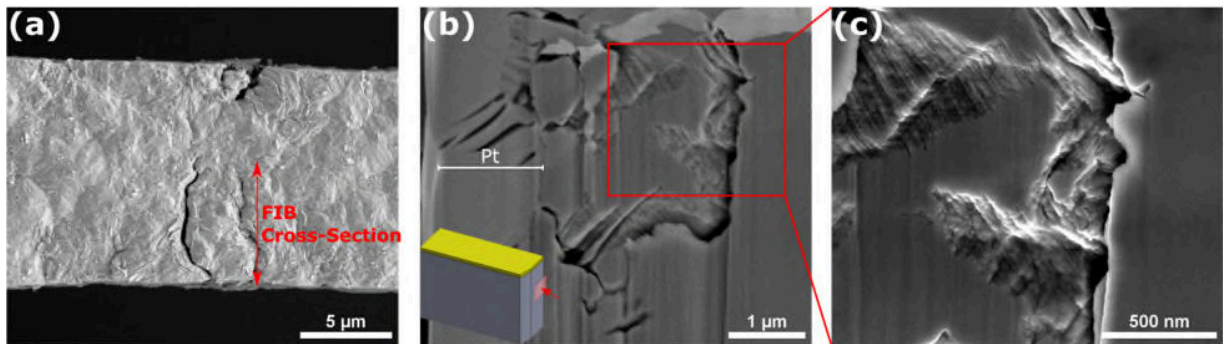

Figure 5. (a) Top view of microbeam showing the location of the FIB cut; (b) Transverse FIB cross-section at the crack; (c) Fatigue striations at the fracture surface

Hence, two independent crack growth rate measurements provide crack growth rates in the 12-20 nm/cycle range in the LCF regime. These values are four orders of magnitude larger than in the HCF/VHCF regime, which exhibits crack growth rates of the order of 10^{-12} m/cycle in air [29]. Additionally, the crack growth rates in the LCF regime are more comparable among rates expected for the growth of microstructurally small cracks. These cracks usually grow meandering tortuous paths through the microstructure with local crack growth rates much larger than those for long cracks and with a streamlined crack front. Hence, our results suggest once more that the

dominating mechanism for crack nucleation and propagation are not equivalent when comparing the two studied regimes.

2.5   Fractography

A series of FIB cross-sections were performed on microbeams tested over a wide range of fatigue lives in order to evaluate the subsurface fatigue damage and to investigate the nanoscale fatigue mechanisms for nucleation and propagation of cracks. Figure 6(a) shows a vertical FIB cross-section of the same microbeam shown in Figure 1(b) and Figure 5 (tested at 79 mrad, $\sigma_a = 715$ MPa, $\varepsilon_a = 0.96\%$ and with $N_f = 680$ cycles), while Figure 6(b) shows a vertical FIB cross-section of a sample tested at 18 mrad (estimated $\sigma_a = 365$ MPa and $\varepsilon_a = 0.21\%$) with $N_f = 3\times10^7$ cycles using the electrostatic technique. Both samples present cracks spanning the thickness of the microbeam that were propagating towards the neutral axis. Figure 6(a) shows two cracks (one extending from the top and another from the bottom) with a fairly straight crack path without many deviations, except at the region where the two cracks meet. In contrast, Figure 6(b) shows a very tortuous crack path and the clear presence of voids, which are linked through thin cracks [29], highlighting again the difference in fatigue crack path behavior between the LCF and HCF/VHCF regimes.
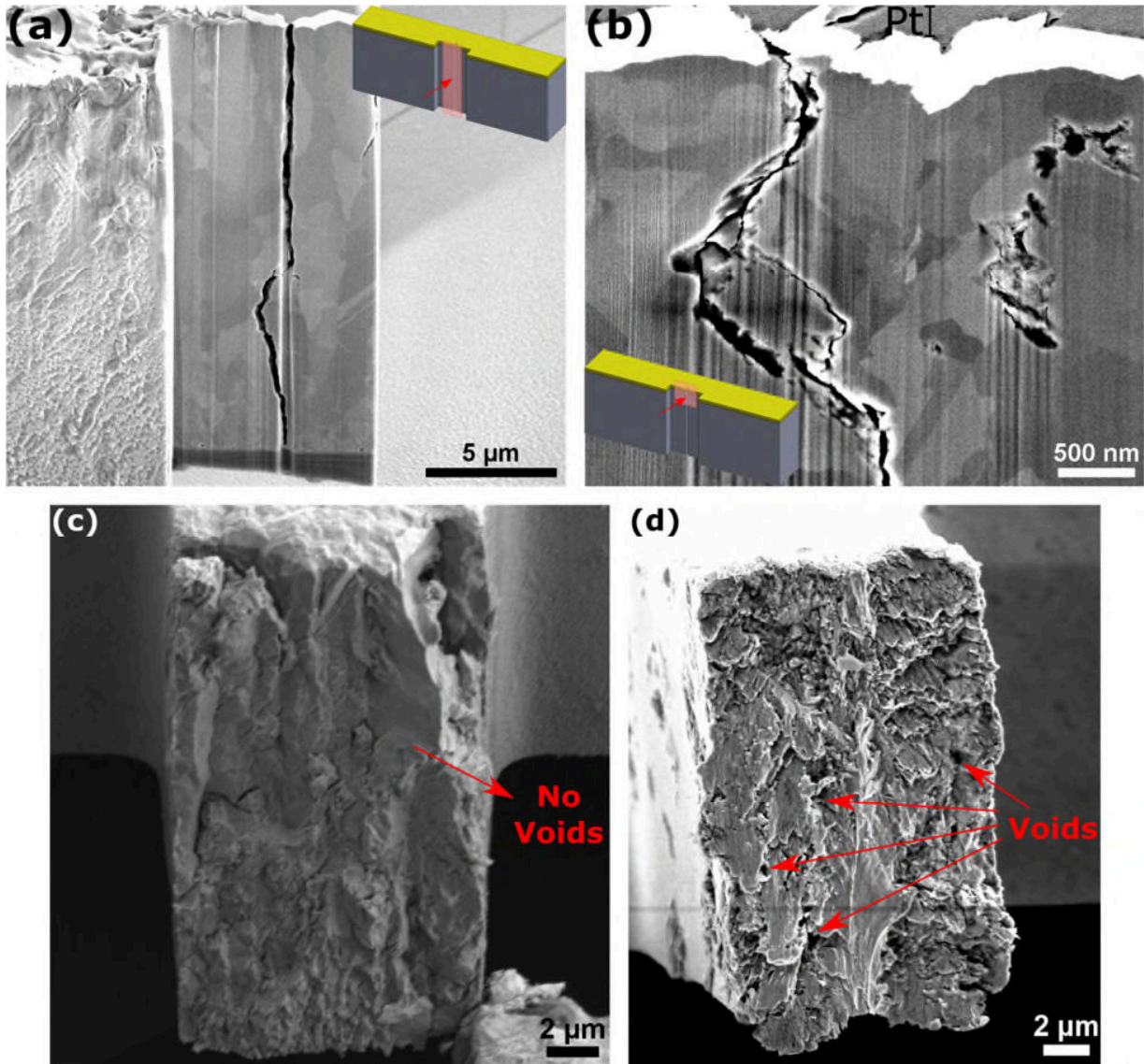
Figure 6. (a) Vertical FIB cross-section of microbeam tested at 79 mrad rotation (estimated $\sigma_a =$ 715 MPa, $\varepsilon_a = 0.96\%$) with the external actuation technique, (b) Vertical FIB cross-section of microbeam tested at 18 mrad rotation (estimated $\sigma_a = 365$ MPa and $\varepsilon_a = 0.21\%$) with the electrostatic technique; Fracture surfaces of samples tested at (c) ~80 mrad rotation (σ_a ~715 MPa and $\varepsilon_a \sim 0.97\%$) and (d) 17 mrad rotation ($\sigma_a = 355$ MPa and $\varepsilon_a = 0.21\%$) with arrows highlighting the presence of voids

Figure 6(c) and (d) show SEM images of the fracture surfaces of two microbeams. Both microbeams exhibited through thickness cracks that spanned almost the whole width of the microbeams (both only had a small remaining ligament around the neutral axis). The fracture surfaces belong to the part of the microbeams that were still attached to the substrate after the careful sectioning of the ligament at the crack surface and removal of the remaining portion of the microbeam. The sample in Figure 6(c) was tested at ~80 mrad (σ_a ~715 MPa and ε_a ~ 0.97%) for N = 1000 cycles using the external actuation technique, while the sample in Figure 6(d) was tested at 17 mrad (σ_a = 355 MPa and ε_a = 0.21%) with N_f = 1.8×10^7 using the electrostatic technique. The fracture surface in Figure 6(c) exhibits a very rugged surface with a zig-zag pattern followed by the crack that propagated towards the middle section of the microbeam, showing what appears to be intergranular crack growth. Figure 6(d) shows a less protruded fracture surface with what seems to be some columnar grains flattened along the crack path. This fracture surface also shows a clear and abundant presence of voids along the crack path, highlighted in the image. These voids are not present in Figure 6(c), confirming than in the LCF regime (high strain amplitudes) the mechanism for crack propagation is no longer controlled by the formation of voids and is instead, controlled by the crack tip stress intensification.

The external actuation technique was also employed to study fatigue samples at lower stress/strain amplitudes although, with tests ran at 0.5 Hz, the runtime of each test significantly increased. One microbeam was tested at 22 mrad (estimated σ_a = 430 MPa and ε_a = 0.26%) and failed with N_f = 3.4×10^5 (same sample as Figure 4(b)). The sample exhibited cracks on both sidewalls that almost spanned the entire width with only a ligament remaining in the neutral axis. A vertical FIB cross-section was performed at a region close to the main crack and is shown in Figure 7 along with high resolution images at areas of interest. The two highlighted areas show portions of a crack that

propagated towards the neutral axis. Voids are clearly observed in these two areas and are very similar to the voids observed in tests using the electrostatic technique. Therefore, this evidence demonstrates that void-controlled crack growth is the main mechanism for crack propagation in this sample. In other words, void-controlled fatigue was observed in samples that were tested under the external actuation technique but at low enough stress/strain amplitudes.
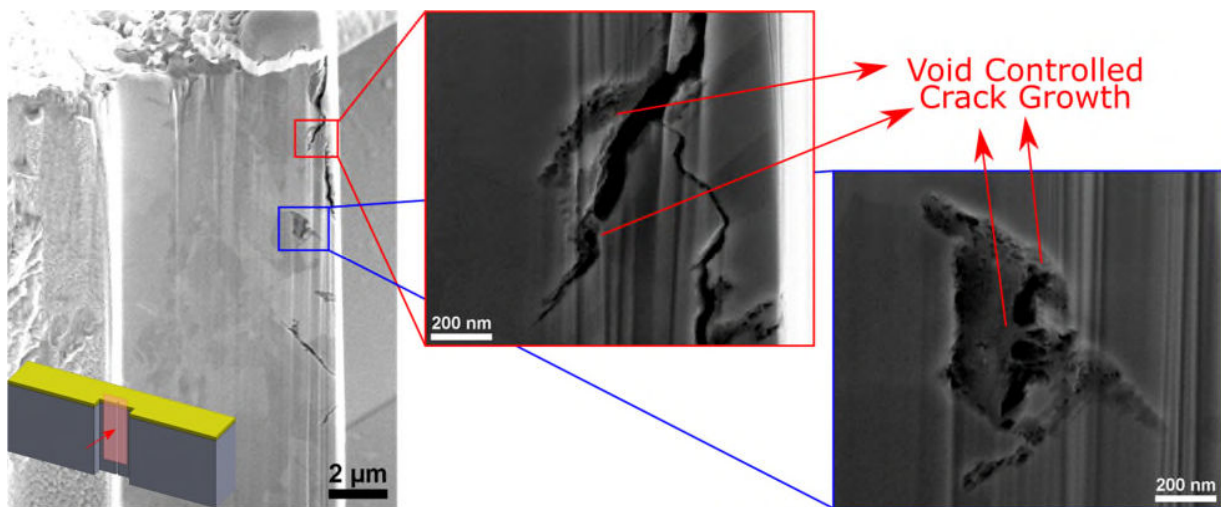

Figure 7. Vertical FIB cross-section showing void dominated crack propagation in microbeam tested at 22 mrad rotation (estimated $\sigma_a = 430$ MPa and $\varepsilon_a = 0.26\%$)

2.6   Discussion

The results of this work highlight pronounced differences in fatigue behaviors and mechanisms for the two studied fatigue regimes. The four orders of magnitude difference in average crack propagation rates and the stress/strain-life curve results with unusual Basquin and Coffin-Manson exponents in the HCF/VHCF due to the extreme stress gradients and more conventional exponents in the LCF regime reveal a transition in the governing fatigue mechanisms from void-controlled mechanisms in the HCF/VHCF to the conventional mechanisms in LCF.

Additionally, in microbeams tested at higher strain amplitudes, the extrusions observed on the sidewalls are much shallower when compared to the ones tested under the HCF/VHCF regime (compare Figure 1(c) with Figure 4(b), respectively). While the microbeam in Figure 4(b) (22 mrad, $\sigma_a = 430$ MPa, $\varepsilon_a = 0.26\%$) shows extrusion heights up to 0.9 µm (measured from top view images), the microbeam in Figure 1(c) (79 mrad, $\sigma_a = 715$ MPa, $\varepsilon_a = 0.96\%$) only show extrusions with a maximum height of 0.4 µm. The extra cycling in the lower strain amplitude ranges with N_f ranging from 10^5 to 10^9 cycles, combined with the void-controlled governing mechanism, contribute to the increase in the average height of extrusions.

The dominating fatigue mechanism in the HCF/VHCF samples with lower applied strain amplitudes is the formation of voids ahead of the crack tip. This mechanism is characterized by ultraslow propagation rates and is likely caused by the prevention of stress concentration effects at the crack tip due to the effect of extreme stress gradients [29]. We therefore show in this work that, once the applied strain amplitudes are large enough, the effects of extreme stress gradients are not as influential and the dominant mechanisms change to the conventional fatigue mechanisms characterized by larger crack propagation rates. This result suggests that there is a threshold in applied strain amplitudes for the change in dominant fatigue mechanisms. The threshold becomes apparent in Figure 3, where there is an inflexion point in fatigue behavior at around $N_f = 10^5$ cycles in the stress/strain-life curves.

At the inflexion point, the two microbeams tested at significantly different frequencies and shown in Figure 4 present void-controlled fatigue as the dominating fatigue mechanism. The lack of frequency effects suggests that the formation of voids is independent of frequency, and therefore the diffusion of environmental species (e.g., hydrogen, oxygen) into the material, thought to be

necessary to stabilize voids resulting from the condensation of vacancies below extrusions or ahead of the crack tip [29], is not the limiting factor governing the overall fatigue process.

Therefore, at N_f higher than 10^5 cycles and at plastic strain amplitudes lower than 10^{-4}, the governing mechanism transitions from the conventional mechanisms in LCF to the void-controlled mechanisms in HCF/VHCF. The void dominated mechanism has been previously observed in the ultrasonic fatigue testing of bulk ultrafine grained Cu [34, 35], although only in the VHCF regime with cycling higher than 10^8 cycles and plastic strain amplitudes lower than 10^{-6}. Hence, the size effects present in the current Ni microbeam study, driven by the microbeam size (dictating the strain gradient under bending), highly influence the transition between the two governing mechanisms, increasing the plastic strain amplitude at which the transition occurs.

3   Conclusions

This work demonstrated an external actuation technique to investigate fatigue behavior of Ni microbeams under bending. Along with a previously reported electrostatic technique, Ni microbeams could be tested over fatigue lives ranging from 100 to 10^9 cycles. Results highlight stark differences in fatigue behavior and mechanisms when comparing LCF and HCF/VCHF. In the HCF/VHCF regime the dominant fatigue mechanism is void-assisted crack nucleation and propagation characterized by ultraslow propagation rates and the fatigue curves are characterized by b = -0.038 and c = -0.30, while in the LCF regime, the dominant fatigue mechanisms are the well-documented fatigue mechanisms characterized by larger crack growth rates and behavior with b = -0.078 and c = -0.57. Results suggest the presence of a threshold in applied strain amplitude around 10^{-4} above which the effects of extreme stress gradients no longer influence the dominant fatigue mechanism. In addition, results highlight the lack of frequency effects in the fatigue behavior of Ni microbeams.

4   Methods

4.1   Experimental Sample

The experimental samples are shown in Figure 8(a). They are microresonator MEMS originally designed for the study of HCF/VHCF and consist of a free-standing Nickel microbeam fixed to the substrate on one side and two arms of interdigitated fingers on the other side [24, 25, 28]. Figure 8(b) shows the microbeam from a top view perspective while Figure 8(c) shows the sidewall. The specimens were fabricated with the MetalMUMPs electrodeposition process from MEMSCAP [36]. The microbeam is composed of a 20 µm structural Ni layer and a thin 1 µm layer of Au on top (see Figure 8(c)). The sidewall of the microbeam (where fatigue damages accumulates) has negligible surface roughness. The microbeam exhibits a fine columnar microstructure (1-2 µm in diameter and 5-10 µm in height) along its thickness with a strong $\langle 001 \rangle$ out of plane texture [28] and has a 0.2% yield stress of ~650 MPa and tensile strength of ~875 MPa, gathered from microtensile testing [25]. The microbeam has dimensions of approximately 60 (length) $\times$ 12 (width) $\times$ 20 (thickness) µm and exhibits a normalized strain gradient of $\eta = \frac{1}{\varepsilon_{max}} \frac{d\varepsilon}{dx} = 17\%$ µm^{-1} [28].
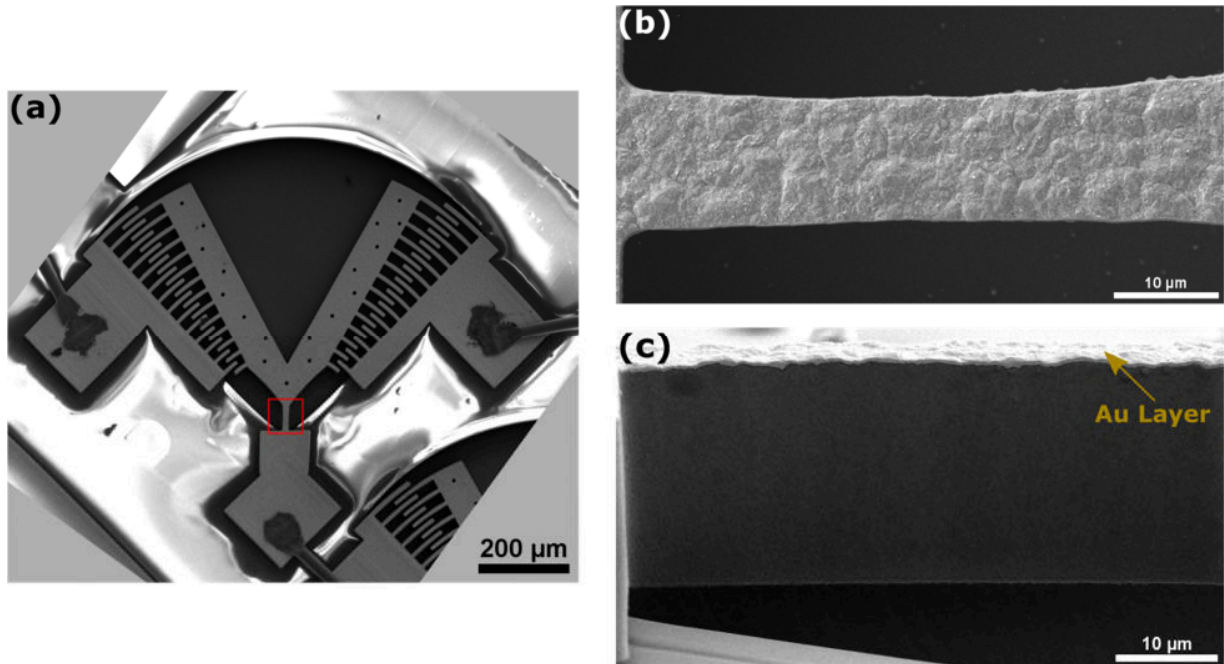
Figure 8. (a) Top view of microresonator, highlighting the microbeam; (b) Top view of

microbeam; (c) Sidewall view of microbeam

4.2 Electrostatic Technique for HCF/VHCF

The electrostatic technique for the study of HCF and VHCF has been extensively described in

previous publications [25-29, 37], hence only a brief review is given here. This technique consists

on the actuation of the microresonators at their resonance frequency (~8 KHz) via electrostatic

forces, which, in turn, causes fully reversed bending fatigue at the microbeam. As fatigue damage

starts to develop in the microbeams sidewalls, the consequent resonance frequency decrease is

tracked periodically during a fatigue test. Therefore, this technique is ideal to study the

HCF/VHCF of small-scale metallic components [28]. The technique was also adapted to

investigate *in-situ* SEM fatigue tests in order to study environmental effects and to allow for more

detailed observations on the evolution of fatigue damage [29].

Figure 9 demonstrates the ranges in applied strain amplitude, ε_a, in which the electrostatic

technique can be applied. Due to experimental limitations on the electrostatic technique and the

damping behavior of the resonators, the maximum applied ε_a is about 0.3%, with plastic strain amplitudes, ε_{pa}, well below 10^{-3} [29]. Therefore, in order to increase the applied deformation on the microbeam and surpass the yield strength, a new external actuation technique was developed.
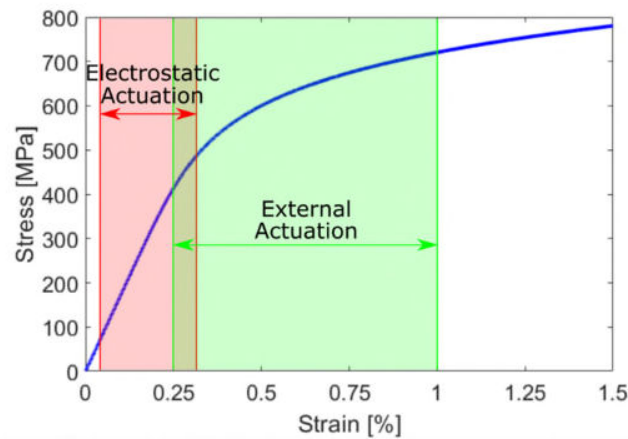

Figure 9. Stress vs strain curve estimated from monotonic tests [27] (see Section 4.4) showing the ranges in which each technique can be employed

4.3   External Actuation Technique for LCF

The external actuation system is depicted in Figure 10(a). The setup consists of a piezoelectric X positioning stage (PI P-611.1) that allows for movement in only one direction. The microresonator is mounted on top of the positioning stage and a Tungsten micromanipulator tip (~50 µm in diameter) is placed and centered between the arms of the microresonator using a manual XYZ positioning stage (Edmund Optics Positioning Stages). The micromanipulator is fixed in space and attached to a calibrated strain-gauge load cell (Transducer Techniques GSO-10) which allows for the measurement of the force required to displace the microresonator. The microresonator and micromanipulator are observed through an optical microscope for initial alignment.
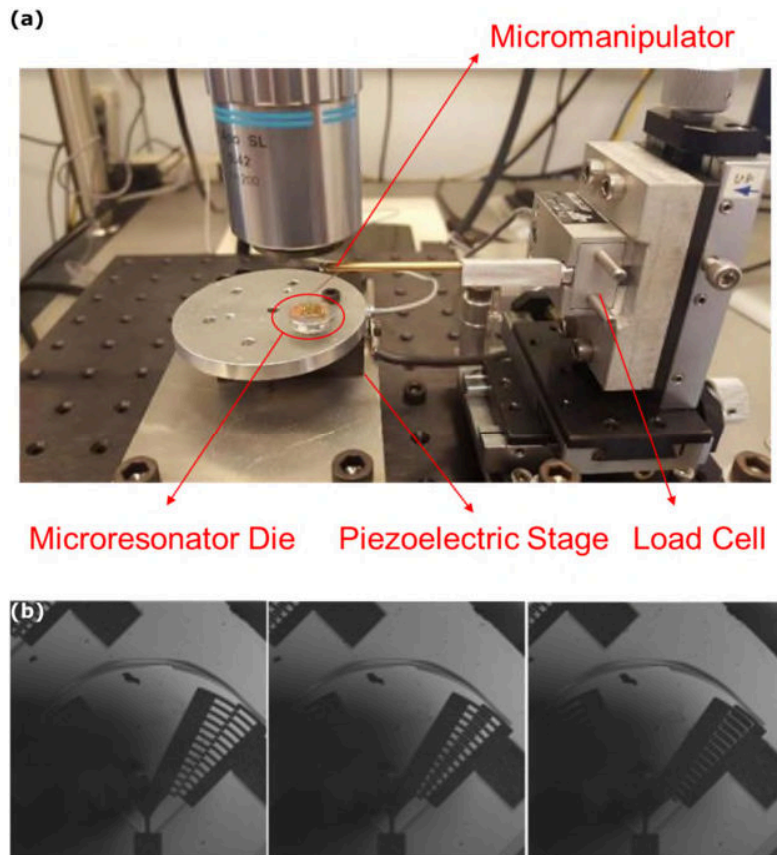
Figure 10. (a) Setup for external actuation technique; (b) Three stages of the microresonator's actuation

The actuation of the microresonator consists of the input of a low sinusoidal voltage into a piezo servo controller (PI E-660) in order to actuate the piezoelectric positioning stage. Once the stage is actuated (along with the microresonator mounted on top), the micromanipulator comes into contact with one arm of the microresonator displacing it by a certain angle of rotation. As the voltage varies and the stage moves in the opposite direction, the micromanipulator releases contact with the arm and, after a short delay, contacts the second arm of the microresonator, also displacing it. Concurrently, the load cell measures the tensile force required to displace the first arm and the

compressive force required to displace the second arm. The actuation of the microresonator for half a cycle is shown in Figure 10(b).

At the beginning of each fatigue test, a few cycles are conducted at a very low frequency and strain amplitude in order to properly align the micromanipulator with the microresonator and ensure symmetric bending loadings on the microbeam. Once a full cycle exhibits the same amplitude for the tensile and compressive forces, the fatigue test is performed at a frequency of 0.5 Hz and at a specified angle of rotation (θ_o) which is measured with the optical microscope (same optical calibration performed in the electrostatic technique with a precision of $\pm$ 0.3 mrad in θ_o) [27]. Therefore, the microbeam attached to the microresonator experiences fully reversed bending fatigue controlled by the rotation angle applied. As the fatigue damage starts to build in the microbeam, the stiffness and, consequently, the measured load amplitude required to displace the microresonator decrease, creating a metric to quantify fatigue damage.

Compared to the electrostatic actuation, the external micromanipulation actuation of the microbeam allows for much higher applied ε_a up to an upper limit of about 1%, as shown in Figure 9. The limit is established by the maximum achievable angle of rotation restricted by the space between the fingers (See Figure 10(b)). This allows for the investigation of metallic components under loadings pertaining to their nominally plastic regime. Therefore, this technique is ideal to study the LCF of small-scale metallic components. The technique can also be used for different R-ratios and at different frequencies ranging from 0.01 Hz to about 200 Hz, although in the current study, only fully reversed loadings and a frequency of 0.5 Hz were used. Additionally, the external actuation allows for the study of the bending fatigue in microbeams at around $\varepsilon_a = 0.3\%$ with 0.5 Hz and the comparison with microbeams tested at about the same ε_a but with ~8 kHz (electrostatic technique) in order to evaluate frequency effects.

4.4 Fatigue Damage Prognosis

The fatigue life, N_f, is defined as the number of cycles to reach a 20% decrease in load amplitude (and therefore rotational stiffness k_θ), which is related to the resonance frequency f_o by the following equation [25, 30]:

$$f_o = \frac{1}{2\pi}\sqrt{\frac{k_\theta}{J_\theta}} \tag{3}$$

where J_θ is the polar moment of inertia. Hence, a 20% decrease in stiffness is equivalent to a 10% decrease in resonance frequency which is the failure threshold used for the electrostatic technique [29]. The maximum stress amplitudes (σ_a) experienced by the microbeams at the beam outer fibers are then calculated from the measured angle of rotation through the correlation, using our previous finite element models [27]:

$$\sigma_a = 24.54 \times 10^3 \theta_o - 2.23 \times 10^5 \theta_o^2 \tag{4}$$

Microstructural sensitive models (Figure 2) [25, 30] have also shown this correlation between the microstructure homogenized maximum stress and the angle of rotation. These models and the calculations presented in Figure 2 follow the constitutive response in Figure 9, which was measured previously with dog-bone microtensile samples. This response follows a Ramberg-Osgood's behavior,

$$\varepsilon_a = \frac{\sigma_a}{E} + \left(\frac{\sigma_a}{H}\right)^{\frac{1}{n}} \tag{5}$$

in which $E = 172\ GPa$ is the Young's modulus, $H = 1451\ MPa$ is the strength coefficient and $n = 0.136$ is the strain hardening exponent.

4.5   Fractography: SEM/FIB Characterization

A dual beam FIB/SEM (FEI Nova Nanolab 200) was used to characterize the extent of fatigue damage in the microbeams. The electron beam was used to characterize the cracks and extrusions/intrusions on the sidewall as well as the cracks on the top surface of the microbeam. FIB cuts were performed with Ga+ ions in order to observe the crack path characteristics in the subsurface of the microbeam. These cross-sections were essential for the interpretation of the underlying mechanisms needed to nucleate and propagate a microstructurally small crack in the Ni microbeams [29]. Before the FIB cuts were performed, a ~1 µm layer of Pt was deposited around the crack region in order to preserve the area of study and to improve the quality of the cuts. The deposition was done at a current of 0.3nA. Rough milling of the microbeam with the ion beam was conducted at a current of 1 nA and polishing milling, at a current of 0.3 nA. FIB cross sections of specimens that only had extrusions/intrusions and others that had reached fatigue failure were performed for samples fatigued under the two techniques described above. Furthermore, three different orientations of FIB cross-sections, in relation to the microbeam, were performed (vertical, horizontal and transverse) [29].

Acknowledgements

Disclosure of potential conflicts of interest

The authors have no relevant financial or non-financial interests to disclose.

References

1. Zhang, G.P. and Z.G. Wang. *Fatigue of Small-Scale Metal Materials: From Micro- to Nano-Scale*. 2008. Springer Netherlands.
2. Licari, J.J. and D.W. Swanson, *Adhesive Bonding Processes*, in *Adhesives Technology for Electronic Applications (Second Edition)*, J.J. Licari and D.W. Swanson, Editors. 2011, William Andrew Publishing: Oxford. p. 143-216.
3. Spearing, S.M., *Materials issues in microelectromechanical systems (MEMS)*. Acta Materialia, 2000. **48**(1): p. 179-196.
4. Krogstad, J.A., C. Keimel, and K.J. Hemker, *Emerging materials for microelectromechanical systems at elevated temperatures*. Journal of Materials Research, 2014. **29**(15): p. 1597-1608.
5. Connolley, T., P.E. McHugh, and M. Bruzzi, *A review of deformation and fatigue of metals at small size scales*. Fatigue & Fracture of Engineering Materials & Structures, 2005. **28**(12): p. 1119-1152.
6. Warnasch, A. and A. Killen. *Low cost, high G, Micro Electro-Mechanical Systems (MEMS), Inertial Measurements Unit (IMU) program*. 2002. Palm Springs, CA: Institute of Electrical and Electronics Engineers Inc.
7. Sparks, D.R., M.I. Chia, and G.Q. Jiang, *Cyclic fatigue and creep of electroformed micromachines*. Sensors and Actuators, A: Physical, 2001. **95**(1): p. 61.
8. Cui, W., X. Huang, and F. Wang, *Current Understanding of Fatigue Mechanisms of Metals*, in *Towards a Unified Fatigue Life Prediction Method for Marine Structures*, W. Cui, X. Huang, and F. Wang, Editors. 2014, Springer: Berlin, Heidelberg. p. 31-68.
9. Suresh, S., *Fatigue of materials*. 2001: Cambridge University Press.
10. Yang, Y., et al., *Nanoscale and submicron fatigue crack growth in nickel microbeams*. Acta Materialia, 2007. **55**(13): p. 4305-4315.
11. Boyce, B.L., J.R. Michael, and P.G. Kotula, *Fatigue of metallic microdevices and the role of fatigue-induced surface oxides*. Acta Materialia, 2004. **52**(6): p. 1609-1619.
12. Lavenstein, S., et al., *High frequency in situ fatigue response of Ni-base superalloy René-N5 microcrystals*. Acta Materialia, 2018. **144**(Supplement C): p. 154-163.
13. Lavenstein, S. and J.A. El-Awady, *Micro-scale fatigue mechanisms in metals: Insights gained from small-scale experiments and discrete dislocation dynamics simulations*. Current Opinion in Solid State and Materials Science, 2019. **23**(5): p. 100765.
14. Burger, S., et al., *A novel high-throughput fatigue testing method for metallic thin films*. Science and Technology of Advanced Materials, 2011. **12**(5): p. 7.
15. Merle, B. and M. Goeken, *Bulge fatigue testing of freestanding and supported gold films*. Journal of Materials Research, 2014. **29**(2): p. 267-276.

16. Kraft, O. and R. Schwaiger, *Size effects in the fatigue behavior of thin Ag films.* Acta Materialia, 2003. **51**(1): p. 195.
17. Zhang, G.P., K. Takashima, and Y. Higo, *Fatigue strength of small-scale type 304 stainless steel thin films.* Materials Science and Engineering: A, 2006. **426**(1): p. 95-100.
18. Wimmer, A., et al., *Cyclic bending experiments on free-standing Cu micron lines observed by electron backscatter diffraction.* Acta Materialia, 2015. **83**: p. 460-469.
19. Glushko, O. and G. Dehm, *Initiation and stagnation of room temperature grain coarsening in cyclically strained gold films.* Acta Materialia, 2019. **169**: p. 99-108.
20. Heckman, N.M., et al., *Rethinking scaling laws in the high-cycle fatigue response of nanostructured and coarse-grained metals.* International Journal of Fatigue, 2020. **134**: p. 105472.
21. Howard, C., et al., *The influence of microstructure on the cyclic deformation and damage of copper and an oxide dispersion strengthened steel studied via in-situ micro-beam bending.* Materials Science and Engineering: A, 2017. **687**: p. 313-322.
22. Kiener, D., et al., *Cyclic response of copper single crystal micro-beams.* Scripta Materialia, 2010. **63**(5): p. 500-503.
23. Gabel, S. and B. Merle, *Small-scale high-cycle fatigue testing by dynamic microcantilever bending.* MRS Communications, 2020: p. 1-6.
24. Baumert, E.K., et al., *Fatigue-induced thick oxide formation and its role on fatigue crack initiation in Ni thin films at low temperatures.* Acta Materialia, 2014. **67**(0): p. 156-167.
25. Baumert, E.K. and O.N. Pierron, *Fatigue Degradation Properties of LIGA Ni Films Using Kilohertz Microresonators.* Journal of Microelectromechanical Systems, 2013. **22**(1): p. 16-25.
26. Sadeghi-Tohidi, F. and O.N. Pierron, *Extreme stress gradient effects on microstructural fatigue crack propagation rates in Ni microbeams.* Applied Physics Letters, 2015. **106**(20): p. 201904.
27. Sadeghi-Tohidi, F. and O.N. Pierron, *Extreme stress gradient effects on the fatigue behavior of Ni notched microbeams.* Acta Materialia, 2016. **106**: p. 388-400.
28. Sadeghi-Tohidi, F. and O.N. Pierron, *Towards prediction of the fatigue life of Ni microbeams under extreme stress gradients.* Extreme Mechanics Letters, 2016. **9**: p. 97-107.
29. Barrios, A., et al., *Quantitative in Situ SEM High Cycle Fatigue: The Critical Role of Oxygen on Nanoscale-Void-Controlled Nucleation and Propagation of Small Cracks in Ni Microbeams.* Nano Letters, 2018. **18**(4): p. 2595-2602.
30. Kakandar, E., et al., *A computational and experimental comparison on the nucleation of fatigue cracks in statistical volume elements.* International Journal of Fatigue, 2020. **137**: p. 105633.
31. Aktaa, J., et al., *High cycle fatigue and fracture behavior of LIGA Nickel.* Scripta Materialia, 2005. **52**(12): p. 1217-1221.
32. Stanzl-Tschegg, S.E. and B. Schonbauer, *Mechanisms of strain localization, crack initiation and fracture of polycrystalline copper in the VHCF regime.* International Journal of Fatigue, 2010. **32**(6): p. 886-893.
33. Stocker, C., M. Zimmermann, and H.J. Christ, *Localized cyclic deformation and corresponding dislocation arrangements of polycrystalline Ni-base superalloys and pure Nickel in the VHCF regime.* International Journal of Fatigue, 2011. **33**(1): p. 2-9.

34.   Lukas, P., et al., *Fatigue damage of ultrafine-grain copper in very-high cycle fatigue region.* Materials Science And Engineering A-Structural Materials Properties Microstructure And Processing, 2011. **528**(22-23): p. 7036-7040.

35.   Kunz, L., P. Lukas, and L. Navratilova, *Strain localization and fatigue crack initiation in ultrafine-grained copper in high- and giga-cycle region.* International Journal of Fatigue, 2014. **58**: p. 202-208.

36.   Cowen, A., et al., *MetalMUMPs Design Handbook.* 2002.

37.   Baumert, E.K. and O.N. Pierron, *Very high cycle fatigue crack initiation in electroplated Ni films under extreme stress gradients.* Scripta Materialia, 2012. **67**(1): p. 45-48.